POLYMER FILMS WITH ION-SYNTHESIZED COBALT AND IRON NANOPARTICLES: CONDUCTANCE AND MAGNETISM

Vladimir N. Popok

Department of Physics and Nanotechnology, Aalborg University, 9220 Aalborg Øst, Denmark

Abstract. The current paper presents an overview and analysis of data obtained on a few sets of polymer samples implanted by iron and cobalt. The low-energy (40 keV) implantations were carried out into polyimide and polyethyleneterephthalate with fluences between 2.5×10^{16}-1.5×10^{17} cm^{-2}. The samples were studied using several different methods to obtain information on structural and compositional changes as well as on the evolution of electrical and magnetic properties. High-fluence implantation led to significant carbonization of the polymers and formation of metal nanoparticles in the shallow layers. Correlation between the structural changes, nucleation and percolation of the particles in relation to electronic properties of the composites are found, described and analysed. A few models explaining electrical and magnetic properties of the polymer films with synthesized metal nanoparticles are suggested.

1. INTRODUCTION

Finite in size particles incorporated into a dielectric medium largely affect the macroscopic properties of the composite, giving rise to a variety of new phenomena [1-3]. Electron transport and magnetic properties of such nanocomposite systems are of both fundamental interest and importance for practical applications, for instance, in the new generation of information storage devices and technologies for magnetic sensors [4,5]. Among the wide range of dielectrics the organic-based materials attract considerable attention to be used in spintronics and as magnetic media [6,7].

Ion implantation is one of the widely-used methods to synthesize nanoparticles (NPs) in a medium [8]. For NPs nucleation the metal concentration must overcome the solubility limit in the given material. Thus, high-fluence implantation is required. If the implantation is carried out into a polymer the high fluences leads not only to the accumulation of metal and particle nucleation but also to significant damage of the material due to the ion stopping and relatively low resistance of polymers with respect to irradiation [9-11]. For low-energy (keV-range) implantation the nuclear stopping dominates, thus, causing structural evolution of an organic matrix. Since most polymers are carbon-based, the implantation leads to degasing of volatile compounds (due to the breakage of chemical bonds) and carbonization of the matrix [10,12,13]. The increase of carbon concentration, scission of polymer chains and cross-linking change the electronic properties and charge transport mechanisms. The high metal concentration and formation of metal NPs contribute to the increase of electrical conductance and can cause the insulator-to-metal transition (IMT) [14,15]. If the embedded metal is a magnetic species the electronic structure of the composite becomes even more complicated. Conductance of such composites can be varied by an external magnetic field caus-

Corresponding author: Vladimir N. Popok, e-mail: vp@nano.aau.dk

ing spin-dependent transport [16]. Magnetic properties of polymer composites with NPs evolve from superparamagnetism towards ferromagnetism with increase of the implantation fluence [17]. Thus, study of electron transport mechanisms and magnetic behaviour of nanostructured polymer media is of great interest to give insights into quantum effects influencing electronic states, magnetoresistance and spin-dependent phenomena.

Current paper gives an overview and comprehensive analysis of the earlier published results on the electrical and magnetic properties of polyimide (PI) and polyethyleneterephthalate (PET) implanted by 40 keV Fe^+ and Co^+ ions [16-26].

2. METAL ION IMPLANTATION

2.1. Implantation conditions

Thin (40 μm) PI and PET foils were implanted by 40 keV Co^+ and Fe^+ ions with fluences $F = 2.5 \times 10^{16}$-1.5×10^{17} cm^{-2} at ion current densities j of 4, 8 and 12 $\mu A \times cm^{-2}$ in a residual vacuum of 10^{-5} Torr. High density of current was used to decrease the time of treatment, i.e. to optimize the implantation regimes for practical applications. To avoid thermal degradation, the sample holder was water-cooled and the temperature of the samples under implantation did not exceed 370K which is much lower than the glass-transition temperatures for both polymers.

2.2. Experimental techniques

Several methods were applied to study the structure and composition of the implanted polymers. The analysis of in-depth composition was done by *Rutherford back-scattering* (RBS) using 2 MeV α-particles. Topographic images of the implanted surfaces were obtained by *atomic force microscope* (AFM) Dimension 3000 (Digital Instruments) in tapping mode. For the in-plain *transmission electron microscopy* (TEM) measurements ultrathin slices of the polymers were prepared by chemical etching of rare (unimplanted) side of the samples using water mixture of potassium hydroxide, monoethanolamine and triethanolamine. The measurements were carried out by TESLA-BS500 microscope. *X-ray photoelectron spectra* were recorded by a Kratos XSAM 800 spectrometer using Mg $K\alpha_{1,2}$ and Al $K\alpha_{1,2}$ radiations and FRR mode. More details on this method can be found in [18].

To provide ohmic electrical contacts to the implanted layer, the electrodes were deposited on the ends of the samples using silver paste. The *tem-perature dependence of resistance* was measured in the interval of 5-300K using a standard quasi-four-probe method in DC regime. The *magnetoresistance* measurements were carried out at voltages corresponding to linear interval of the current-voltage dependences. Magnetoresistance was calculated as following $MR = \Delta R/R_0 = (R - R_0)/R_0$, where R and R_0 are the values in the presence and absence of the magnetic field, correspondingly. Effect of external magnetic field on the charge carrier transport was studied for two orientations with respect to the foil plane: parallel (in-plane) and perpendicular. In both cases the direction of the applied magnetic field (B) was perpendicular to the direction of electric field or current. B was varied from -5 to 5 T. The measurements were carried out at liquid helium temperature (4.2K).

Ferromagnetic resonance (FMR) spectra of the foils were obtained on *Bruker EMX* Electron Spin Resonance spectrometer at X-band frequency of 9.8 GHz. The FMR spectra were recorded at room temperature and various orientations of implanted surface with respect to the applied DC magnetic field. *Magnetization dependences* were obtained using SQUID XL-5 in the temperature interval of 2-300K for in-plane orientation of the magnetic field. The measurements of the temperature dependence of magnetization M were carried out in two regimes: zero field cooled (ZFC) and field cooled (FC) at $B = 1$ or 10 mT.

2.3. Evolution of polymer structure and composition

Effect of ion implantation on the structure and composition of polymers is a complex of physical and chemical processes originated by interaction of the impacting ions with polyatomic target [27,28]. The processes depend on the energy transferred to the polymer at the ion bombardment, on the composition and structure of virgin polymer and its interaction with the environment after the implantation. There are two main mechanisms of the energy transfer from ions to a polymer which proceeds by nuclear collisions and electron excitations. Since iron and cobalt are chemical elements with relatively high masses and the implantation energy is relatively low, the nuclear stopping dominates. Energy transfer in binary nuclear collisions leads to direct bond breakage. Since the ion energy is much higher than the binding energy of atoms in both polymers, the ion imparts enough energy to the primary replaced atom (recoil) for the following replacements, thus, producing non-linear collision cascades [11,29].
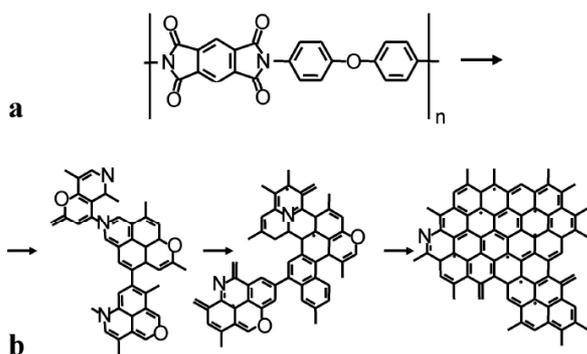
Fig. 1. (a) Chemical formula of PI elementary unit and (b) transformation of the polymer structure upon implantation.

Ion implantation of PI results in both the disruption of phenyl rings and degradation of imide groups yielding such products as iminic and pyridinic-like groups as well as tertiary amines [30, 31]. The scheme of the PI transformation under high-fluence 40 keV Ar^+ ion implantation, proposed in [32], shows the formation of extended polycondensed structures (see Fig. 1). One can assume that the evolution of PI under the implantation of Fe^+ and Co^+ ions is qualitatively the same. In the case of PET implantation, the polymer chains can lose $-CH_2-$ and $-O-CH_2-$ groups as shown in Fig. 2 that leads to efficient formation of conjugated bonds [33,34].

Under the high-fluence implantation the individual radiation cascades significantly overlap and a lot of energy is transferred to the matrix, thus, heating the polymer. Radiative- and thermal-induced processes interplay in a complex manner. They are often represented as a unified phenomenon of radiothermolysis. In our case of 40 keV implantation energy, the thickness of the modified layer was estimated to be ca. 100 nm in both polymers and for both implantation species [18,21]. This fact is related to the small difference in masses of cobalt and iron as well as to very close densities of PI and PET. For the PI samples it was shown using RBS and XPS [18,21] that there is significant depletion of nitrogen and oxygen in the shallow layer which was a consequence of the degassing, i.e. escape of the volatile compounds realized in the radiothermolysis process. Typical molecules and fragments emitted by implanted PI are H_2, C_2H_2, CO, and CO_2 [35]. It is worth noting that very similar thicknesses of the modified layers were recently obtained by independent studies of 40 keV implantation of Co and Ni in PI, PET, and polyetheretherketone [36,37]. These publications also showed significant hydrogen and oxygen depletion in the shallow layers of these polymers.

Direct consequence of the degassing is an increase of carbon ratio in the implanted layer, i.e. carbonization of polymers [13,27]. Carbonization process is dependent on type of polymer and its structure. The carbon-enriched zones are initially formed in the latent tracks [38]. With fluence increase, the π-bonded carbon clusters grow and aggregate forming the network of conjugated C=C bonds. The process of the ion-induced carbonization under implantation of heavy ions is practically accomplished at fluence level of $(1-5)\times10^{15}$ cm^{-2} [27, 39]. Thus, for the different fluences in the interval 10^{16} - 10^{17} cm^{-2} one can expect about the same carbon ratio in the implanted layer. When the initial content of carbon is high, as in the case of PI (56 at.%), the carbon concentration in the shallow surface layer can reach ca. 85-90 at.% after the high-fluence treatment [40]. In other words, one can assume the growth of a quasi-continuous carbonaceous layer under the polymer surface [41] which can even be transformed into the phase mostly consisting of amorphous carbon or graphite-like material [42].

2.4. Metal depth profiles and formation of NPs

The formation of NPs in polymers was realised at the beginning of the 80's by Koon and co-workers [43,44] in their experiments on high-fluence implantation of Fe^+ ions. Threshold fluence at which the particles start nucleating was found to be about 1×10^{16} cm^{-2} for majority of polymers. Assuming that the NP growth occurs by successive joining of the
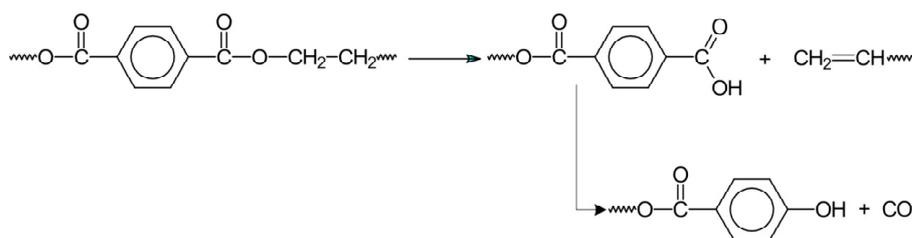
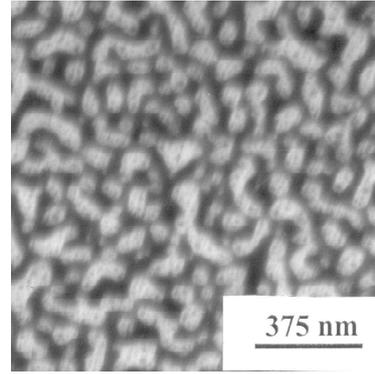**Fig. 2.** Structural transformation of PET under implantation.
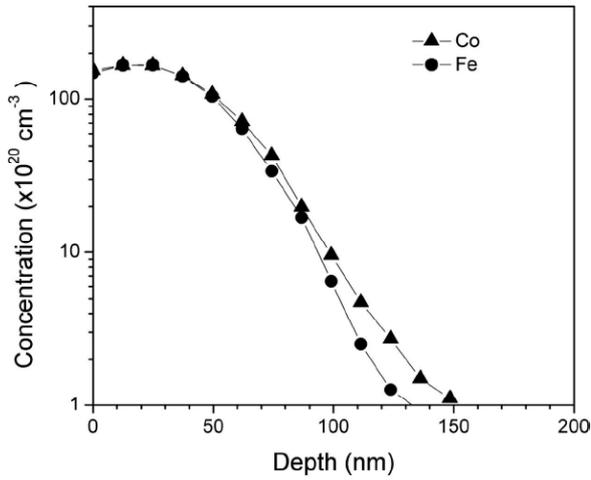
Fig. 3. Depth distribution profiles of cobalt and iron implanted into PI with fluence of 1.25×10^{17} cm^{-2} at $j = 4$ μA$\times$cm^{-2}.

Fig. 4. In-plane TEM image of PET implanted by 40 keV Fe$^+$ ions with fluence of 1.25×10^{17} cm^{-2} at $j = 4$ μA$\times$cm^{-2}. Iron structures are shown in darker shade.

single atoms one can conclude that the process is governed by both the local concentration of metal and diffusion coefficient. The particles nucleated at fluencies just above the threshold one are usually spherical in shape. However, the statistically non-uniform distribution of the metal atoms over the depth leads to a size dispersion of NPs. Typical depth distribution profiles for the implanted Co and Fe in PI are shown in Fig. 3. As one can see, the maxima are located at very low depth. Since larger in size particles are formed at the depth corresponding to highest metal concentration, one can expect the majority of NPs to be situated just beneath the surface. For the PI implanted by Co$^+$ ions with $F =$ 1.25×10^{17} cm^{-2} the mean size of the particles was estimated to be on the scale of a few nm and a very few largest NPs did not exceed 20 nm according to the TEM measurements [22]. However, Fe NPs nucleated at the same implantation conditions were found to be much larger with a mean size of ca. 60 nm [19]. In the PET foils implanted with $F = 1.5\times10^{17}$ cm^{-2} the iron NPs formed large agglomerates resulting in labyrinth-like structures as shown by TEM in Fig. 4 [17]. Surface topography of the sample obtained by AFM was found to be in good correlation with this TEM image [17].

3. PROPERTIES OF METAL-IMPLANTED POLYMERS

3.1. Electric conductance

Evolution of the polymer structure and composition under the implantation leads to significant carbonization, formation of conjugated and dandling bonds. Unpaired *p*-electrons become charge carri-

ers [45] and the dominating conductance mechanism was found to be a variable range hopping (VRH) [46]. Since the conducting phase in the implanted layer is formed of the discrete clusters, the conductance has a threshold character showing the percolation transition for the fluence range corresponding to the overlapping of these regions. This percolation behaviour was confirmed by number of publication [9,47,48,49] and discussed in detail, for instance, in [12,27,34]. In our case, the resistance was found to be decreasing with the fluence and at values between 7.5x10^{16} and 1.0x10^{17} cm^{-2} the transition to plateau-like behaviour was observed for the Co-implanted PI and Fe-implanted PET [16,17,25].

Measurements of temperature dependence of conductance can provide exact information on the dominant mechanisms of the charge carrier transport. Conductance of implanted polymers can be well described by the following exponential dependence

$$\sigma(T) = \sigma_0 \exp\left(-\left(T_0 / T\right)^m\right), \qquad (1)$$

where σ_0 is the conductivity at temperature $T \to \infty$ and T_0 is the characteristic temperature which is defined by the density of states at the Fermi level and the size of the region for the electron localisation [46].

The power m is crucial for determining the conduction mechanism. For band conduction in extended states, $m = 1$. If states are not extended but Andersen localisation is throughout the whole band so that any mobility edge is in a higher energy band, a nearest-neighbour hopping occurs which can also lead to a temperature dependence with $m = 1$ [46]. For a truly disordered material, Mott and Devis predicted a VRH mechanism between localised
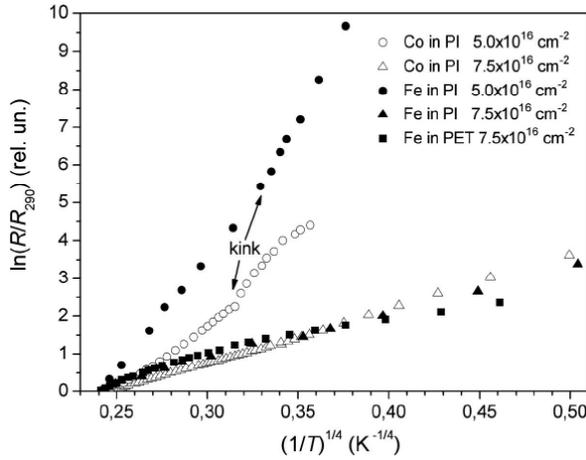
Fig. 5. Temperature dependences of resistance for PI and PET implanted by 40 keV Co$^+$ and Fe$^+$ ions with various fluences at $j = 4$ μA$\times$cm^{-2}.

states [50]. For this mechanism, m has following relation with the dimensionality D

$$m = 1/(1 + D). \qquad (2)$$

A three-dimensional (3D) VRH thus corresponds to $m = 1/4$. 2D and 1D models represent Eq. (1) with the power equal to 1/3 and 1/2, respectively. However, in the disordered material it is difficult to distinguish between the mechanisms of different dimensionality. Therefore, Wang and co-authors [51] suggested the mixed conduction mechanism where

$$\sigma(T) = \sigma_1 + \sigma_2 + \sigma_3 = \sigma_{01} \exp\left(-\left(T_{01}/T\right)^{1/2}\right) +$$
$$\sigma_{02} \exp\left(-\left(T_{02}/T\right)^{1/2}\right) + \sigma_{03} \exp\left(-\left(T_{03}/T\right)^{1/4}\right), \qquad (3)$$

which gives reasonable agreement with the experimental results and allows calculating average characteristic temperatures and activation energies.
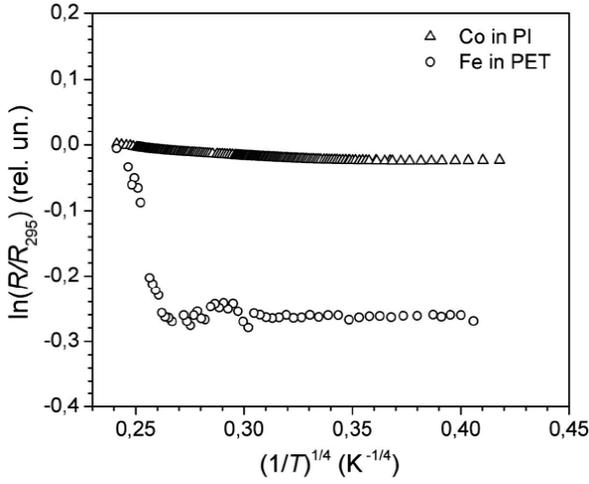
It was found that temperature dependences of resistance for the Co-implanted PI and Fe-implanted PI and PET in the fluence interval of $(2.5-7.5)\times10^{16}$ cm^{-2} can be well extrapolated by linear functions in coordinates $R - (1/T)^{1/4}$. Thus, one can suggest 3D VRH to be a dominant mechanism for the conductance. A few selected dependences are shown in Fig. 5. Some of the curves experience a kink at low temperatures. One can suggest that these transitions are related to the contribution of metal NPs to the charge transport, in particular, to the change of electronic structure at given temperatures. These phenomena will be discussed in more detail below in the part about magnetoresistance. It is worth noting that for fluence 7.5×10^{16} cm^{-2} the curves almost coincide for both

ion species and both types of polymers (the deviation becomes considerable at $T < 40K$). These is an evidence for about the same level of radiation-induced changes of the structure providing very similar conditions for the charge carrier transport despite the initial difference in polymer structure and composition. In other words, the conductance is governed by the implantation-induced carbonization and the contribution of the implanted metal is minor.

The increase of fluence leads to significant rise of metal concentration (filling factor) in the implanted layer. To analyze electrical conductance of these samples the phenomenon of percolation of the metal inclusions must be taken into account. According to commonly-accepted theories of electronic transport in percolating materials, the bulk conductivity of a metal/insulator composite near the IMT can be given by the power law

$$\sigma = \sigma_0 \left(\varphi - \varphi_c\right)^t, \qquad (4)$$

where ϕ and ϕ_c are the normalised metal concentration and the critical concentration corresponding to the percolation, respectively. For the percolation regime, exponent t is predicted to be less than 2 [52]. Percolation threshold varies from one type of composite to another. In the literature one can find typical ϕ_c values between 0.1 and 0.5. The transition to percolation in conductance changes the character of the temperature dependence of resistance. For our samples it occurs at $F = 1.25\times10^{17}$ cm^{-2} which corresponds to metal filling factor of ca. 25 at.% [18] or $\phi_c = 0.25$. In Fig. 6 one can see the dependences obtained for PI implanted by Co$^+$ ions with fluence of 1.25×10^{17} cm^{-2} at ion current density of 12 μA/cm^2 and PET implanted by Fe$^+$ ions with the same fluence but at lower ion current density of 4 μA/cm^2. These dependences are very different compared to those shown in Fig. 5. Both curves have positive temperature coefficient of resistance contrary to the case presented in Fig. 5 where this coefficient is negative. This is typical for disordered (granular) metal films and indicates the IMT for the samples implanted with high fluences. In other words, the samples of Fig. 5 are on the "dielectric side" of the transition while those of Fig. 6 are on the "metallic side". This difference is clearly seen in Fig. 7 where the temperature dependence of activation energy is shown for two PI samples on the different sides of IMT. The sample on the "dielectric side" has negative slope while the one on the "metallic side" demonstrates the positive slope. The IMT is caused by the increased metal concentration and percolation transition. In these samples the phe-

Fig. 6. Temperature dependences of resistance for PI implanted by Co$^+$ ions with fluence of 1.25×10^{17} cm^{-2} and for PET implanted by Fe$^+$ ions with fluence of 1.0×10^{17} cm^{-2}. $j = 4$ μA$\times$cm^{-2} for both cases.
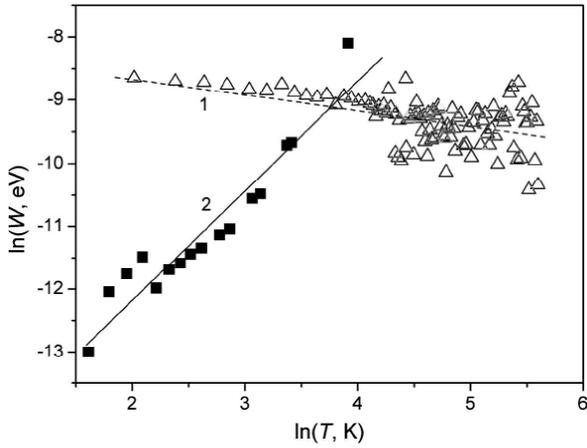

Fig. 7. Temperature dependences of local activation energy for PI implanted by Co$^+$ ions with (1) fluence of 7.5×10^{16} cm^{-2} at $j = 4$ μA$\times$cm^{-2} and (2) fluence of 1.25×10^{17} cm^{-2} at $j = 12$ μA$\times$cm^{-2}.

nomena of weak electron localization and electron-electron interaction [14,53,54] significantly contribute to the charge carrier transport and it can not be described only through VRH. Following equation was suggested in [55] for the semimetallic behavior of conductance

$$\sigma(T) = \sigma_0 + aT^{1/2} + b\ln\left[\sinh\left(T/c\right)^{3/2}\right], \qquad (5)$$

where σ_0 is the contribution of classical Drude conductance, the second and third terms represent the quantum correction due to the weak electron localization and electron-electron interaction with a, b and c to be the fitting parameters. For the case when $T << c$ one obtains the low-temperature asymptote and Eq. (5) transforms to
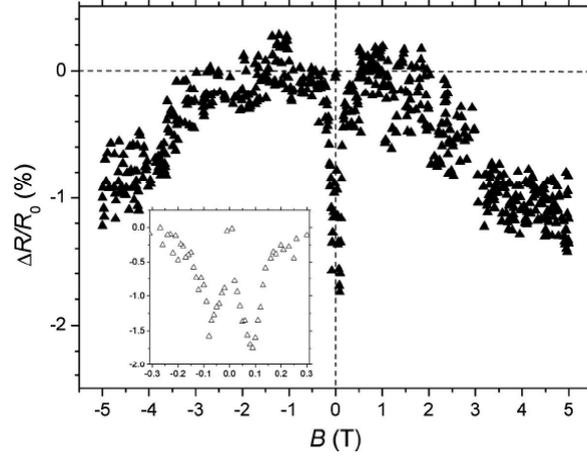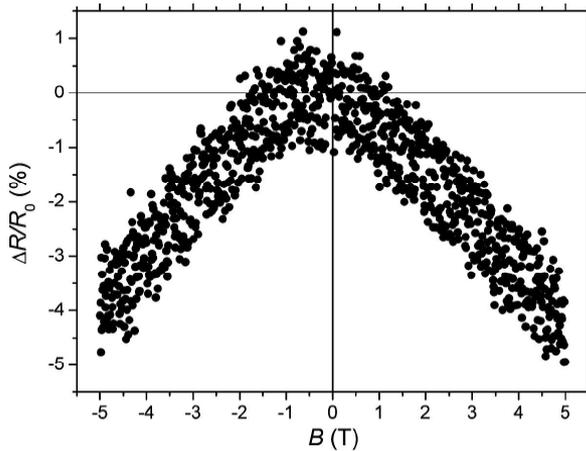

Fig. 8. Dependence of magnetoresistance on applied magnetic field for PET implanted by Fe$^+$ ions with fluence of 7.5×10^{16} cm^{-2} at $j = 4$ μA$\times$cm^{-2}. Insert shows zoom into low field interval. Measurements are performed at 4.2K.

$$\sigma(T) = \sigma_0' + \alpha T^{1/2} + b'\ln T. \qquad (6)$$

The fitting prepared by this equation showed good agreement with the experimental curves for the Co-implanted samples on the "metallic side" [23].
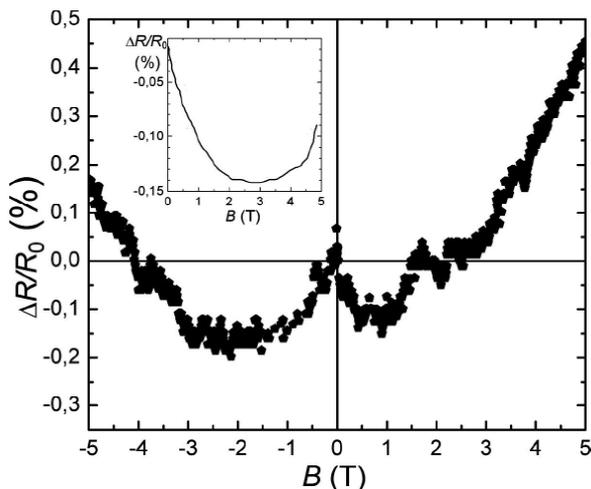
3.2. Magnetoresistance

Since iron and cobalt are ferromagnetic materials in bulk, magnetic properties of the formed NPs can affect the conductance of the samples in an external magnetic field. For both the cobalt-implanted PI and iron-implanted PET very similar magnetoresistive dependences were found for the samples on the "dielectric side" of IMT. As typical example, one can see the dependence of MR on the external magnetic field for the PET implanted by Fe$^+$ ions with $F = 7.5 \times 10^{16}$ cm^{-2} in Fig. 8 [25]. This dependence corresponds to in-plane configuration. One can clearly see general tendency of MR to decrease with increasing field that can be explained by considering interference processes for VRH electrons [53], which is the dominating mechanism of conductance for the samples on the "dielectric side". However, closer look at the dependence in weak magnetic field (see insert to Fig. 8) demonstrates presence of minima at around 70-80 mT. For the Co-implanted PET these minima were found at ca. 115 mT [26]. It was suggested that they are related to the change in magnetic structure of the metal/polymer composites under the applied magnetic field. This phenomenon will be discussed in section 3.3 in relation to magnetic properties of the implanted polymers.

Fig. 9. Dependence of magnetoresistance on applied magnetic field for PET implanted by Fe^+ ions with fluence of 1.0×10^{17} cm^{-2} at $j = 4$ $\mu A \times cm^{-2}$. Measurements are performed at 4.2K.

The dependences for samples on the "metallic side" are different for the cases of iron and cobalt. The one for the Fe-implanted PET is shown in Fig. 9 [25]. The dependence is monotonous and there is a decrease of *MR* for a few percent with increasing field. This behavior is similar to that observed for the granular films prepared by evaporation [56]. However, there is no evidence for a giant magnetoresistance (GMR) which is quite typical for ferromagnetic materials. It can be suggested that GMR is suppressed by an anisotropic magnetoresistive (AMR) effect due to inhomogeneous distribution of magnetic particles in the implanted layer, severe


Fig. 10. Dependence of magnetoresistance on applied magnetic field for PI implanted by Co^+ ions with fluence of 1.25×10^{17} cm^{-2} at $j = 12$ $\mu A \times cm^{-2}$ for perpendicular orientation of the field. Insert shows the dependence for in-plane orientation of the field. Measurements are performed at 4.2K.

radiation damage and significant carbonization of the surrounding polymer matrix.

The dependence obtained for the Co-implanted PI is shown in Fig. 10 [26]. One can see that *MR* decreases with increase of *B* reaching an extreme. At high values of *B*, *MR* becomes positive but only for perpendicular orientation of the field to the sample plane. As can be seen in the insert, *MR* also goes through minimum but it is still negative for in-plane orientation of the magnetic field. Thus, it can be concluded that there is a competition of the negative and positive magnetoresistive effects. Damping of the processes of weak electron localization by the external magnetic field and AMR effect give main contributions into negative *MR* component while conventional Lorentz magnetoresistance is responsible for the positive component. The asymmetry of the dependence (in positive and negative magnetic field) is most probably caused by the inhomogeneous distribution of Co NPs in the sample plain and related nonuniformity of the magnetic structure of the composite film. This effect of nonuniformity is much stronger in the Co-implanted PI compared to the Fe-implanted PET. One of the reasons can be related to the difference in NP formation. As mentioned in section 2.4, cobalt particles are much smaller and more disperse, their magnetic interaction is much weaker (this will be discussed in section 3.3) and, therefore, in high magnetic fields one can observe anomalous increase of *MR*. This suggestion is supported by the fact that decrease of magnetoresistance is much stronger in the iron case reaching ca. 4% for 5 T (see Fig. 9) while in the case of cobalt it is only a fraction of percent (see Fig. 10), i.e. the *MR* variation is very small. It is worth noting that the obtained results on magnetoresistive effect are in agreement with the data published by Chen et al. on PI implanted by 80 keV Co^+ ions with fluences of 1.25×10^{17} and 1.75×10^{17} cm^{-2} [57]. They suggested the spin-dependent tunneling and suppression of an inelastic spin-dependent scattering of conduction electrons to be dominant mechanisms originating the magnetoresistive effect.

3.3. Magnetic properties

For the case of iron and cobalt, the ensemble of metal NPs formed in the implanted layer may behave as a thin film of ferromagnetic continuum due to magnetic dipolar coupling between the particles. The magnetic properties of the implanted polymer films were studied using FMR measurements [17,19,22]. The intensity of FMR signal changes with fluence
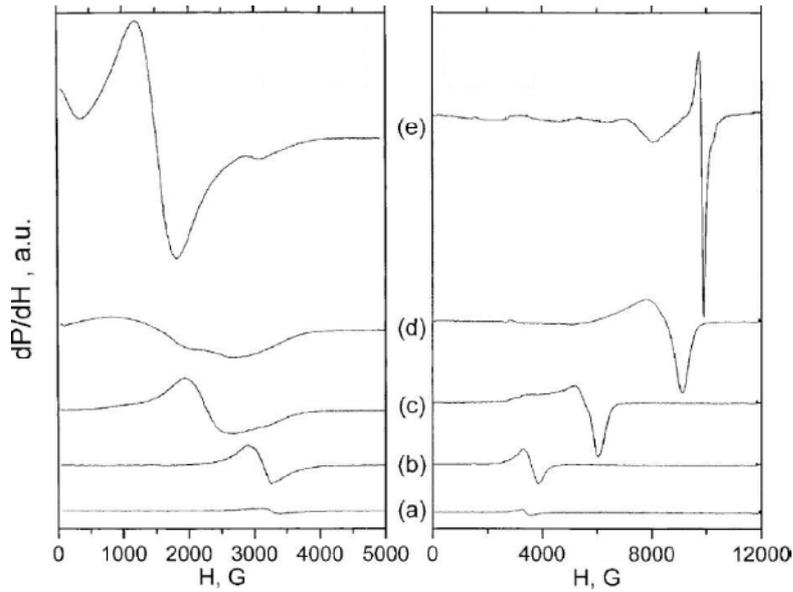
Fig. 11. FMR spectra for PI implanted by Fe^+ ions with fluences of (a) 2.5×10^{16}, (b) 5.0×10^{16}, (c) 7.5×10^{16}, (d) 1.0×10^{17}, and (e) 1.25×10^{17} cm^{-2}. $j = 4$ $\mu A\times$cm^{-2} for all cases. Left panel corresponds to in-plane orientation of the field, right panel - to the perpendicular one.

and the spectra gains strong anisotropy as one can see by the example of iron-implanted PI shown in Fig. 11. The phenomenon qualitatively resembles the anisotropic behaviour of FMR signal of continuous thin magnetic films, where the value of resonance field depends on the film orientation in the magnetic field [58]. Measurements of angular dependence of the effective anisotropy allow concluding that the metal-implanted polymers exhibit uniaxial out-of-plane type of anisotropy; magnetization of the composite layer is directed in plane with the surface [7]. From hysteresis behaviour of FMR spectra effective magnetization values M_{eff} were found for the implanted samples [17,19,22]. They are summarized in Fig. 12. One can see that at $F >$ 5.0×10^{16} cm^{-2} there is a significant increase of M_{eff} which indicates the percolation transition corresponding to strong magnetic coupling of NPs. According to the calculations based on the measured magnetic properties [22] the metal filling factor of cobalt in PI is about 0.14 for $F = 7.5\times10^{16}$ cm^{-2} and it rises up to ca. 0.24 for $F = 1.0\times10^{17}$ cm^{-2}. These values are in a good agreement with the filling factors obtained using RBS for both iron- and cobalt-implanted polymers [18]. Hence, one can conclude that the magnetic percolation transition occurs at much lower level compared to that which is required for physical percolation of NPs or percolation transition in conductance which is described in section 3.1. The decrease of M_{eff} for the cobalt-implanted PI with the fluences above 1.0×10^{17} cm^{-2} was suggested to be not due to the decrease of the filling factor but

due to the evolution of the polymer structure, in particular the strong carbonization. The implanted Co atoms can react with carbon yielding the formation of non-magnetic Co_3C and Co_2C carbides [59,60]. One more possible reason could be Co inward diffusion [15] and Ostwald ripening of Co NPs [61]. Combination of these two processes would facilitate reduction of the mean particle sizes and increase in the size dispersion, thus, dumping the magnetic ordering and weakening the magnetic coupling.

The estimation of the magnetic percolation transition was found to be in good agreement with the SQUID measurements. In Fig. 13 one can see ZFC
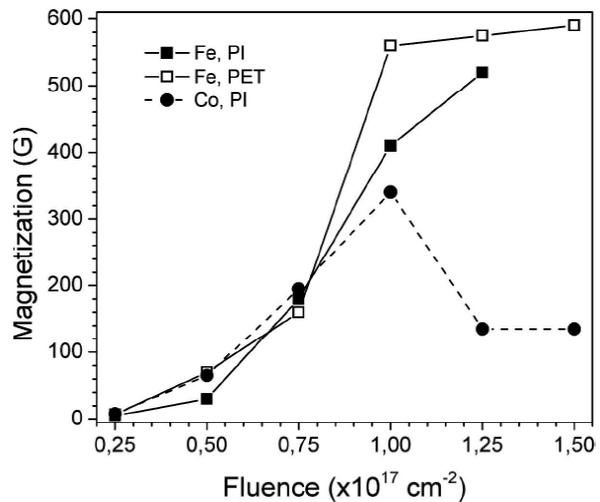
Fig. 12. Magnetization as a function of implantation fluence for Fe- and Co-implanted PI as well as for Fe-implanted PET. $j = 4$ $\mu A\times$cm^{-2} for all cases.
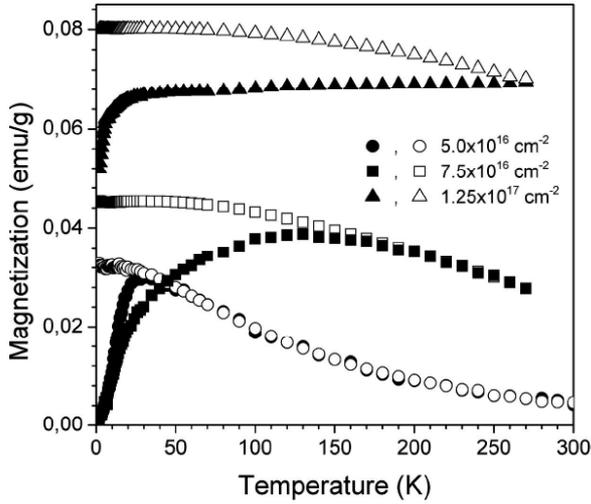
Fig.13. Temperature dependence of ZFC (filled symbols) and FC (open symbols) magnetizations for PET implanted by Fe+ ions with various fluences at $j = 4$ μA×cm^{-2}. Measurements are performed for applied field of 10 mT.

and FC magnetization data as a function of temperature for different fluences of Fe+ ions implanted in PET. Narrow peak at $T_b \approx 30$K (T_b is a blocking temperature) of ZFC curve for $F = 5.0´10^{16}$ cm^{-2} indicates that the magnetic moments of NPs are "frozen" in random directions at temperatures below T_b, i.e. the composite exhibits ferromagnetic properties. Above T_b, the system is in superparamagnetic regime and the temperature dependence of magnetization is found to be close to Langevin law

$$M = M_s \left[\coth \alpha - 1/\alpha \right], \qquad (7)$$

where M_s is the saturation magnetization and $\alpha = \mu_p B / k_B T$, where μ_p is the mean magnetic moment of a particle and k_B is the Boltzmann constant. We used Fe bulk cubic anisotropy constant $K \approx 5.5 \times 10^4$ J m^{-3} at low temperature to estimate an upper limit for the iron particle sizes. Using the relation [26]

$$K_{eff} V = 25 k_B T_b, \qquad (8)$$

where $K_{eff} = K/4$ in the case of randomly oriented single-domain spherical particles with body-centered cubic symmetry and V is NP's volume, the limiting value of particle diameter was found to be ca. 12 nm. Further increase of fluence led to broadening of ZFC peak and shift to higher $T_b \approx 130$ K (7.5×10^{16} cm^{-2}). It can be seen that FC curve became almost flat at low temperatures (< 50K). These dependences indicated an increase of the particles sizes and stronger magnetic coupling. At higher fluences, the temperature of magnetic irreversibility T_s (when ZFC and FC curves split) approached room

temperature (see Fig. 13) that is known to be typical for magnetic granular systems with wide particle size distribution and strong magnetic interaction [62]. Thus, one can conclude about a transition to ferromagnetic-like behavior due to further increase of NPs in size and their agglomeration at iron fluences $\geq 7.5 \times 10^{16}$ cm^{-2}.

Magnetization data as a function of temperature for the cobalt-implanted PI are shown in Fig. 14. For the lowest fluence of 5.0×10^{16} cm^{-2}, $T_b \approx 9$K and FC curve can be pretty well approximated by Eq. (7) indicating the formation of very small NPs with negligible magnetic coupling. Increase of the fluence leads to increase of magnetization, rise of T_b and T_s. For the highest fluence of 1.25×10^{17} cm^{-2} one can observe the plateau on ZFC curve below 50K. By analogy with the iron-implanted PET one can conclude about the transition to ferromagnetic ordering. However, contrary to the iron case, in the cobalt-implanted PI the magnetic coupling of NPs is much weaker and the samples are superparamagnetic above the blocking temperature even for the highest fluence.

Using SQUID measurements the coercive field H_c was measured for all Co-implanted PI samples at 4.5K, i.e. for the composites in the ferromagnetic state. It was found that H_c increases with fluence that is in good agreement with the above conclusion about the transition to ferromagnetic ordering. It is interesting to compare the obtained values of H_c with the field (magnetic induction B_m) values at which local minima in the magnetoresistive dependences
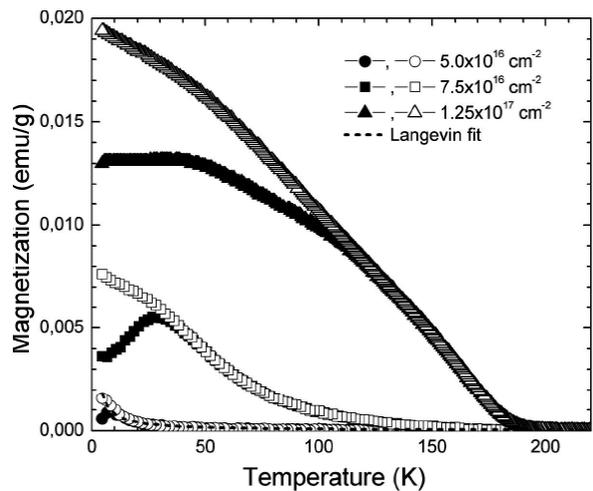
Fig. 14. Temperature dependence of ZFC (filled symbols) and FC (open symbols) magnetizations for PI implanted by Co+ ions with various fluences at $j = 4$ μA×cm^{-2}. Measurements are performed for applied field of 1 mT. Dashed line represents the fit for the lowest fluence using Langevin function.

were found for the samples on "dielectric side" of IMT (see section 3.2). For instance, for the sample implanted with $F = 7.5 \times 10^{16}$ cm^{-2} at $j = 4$ μA×cm^{-2} $B_m \approx 115$ mT while $H_c = 78$ Oe that corresponds to $B = 7.8$ mT. Similar large differences were observed for other fluences. It is worth mentioning that the same order of difference between H_c and B_m was found for the iron-implanted PET. Thus, this is one more fact supporting the above conclusion that magnetic interaction of metal particles leading to ferromagnetic ordering (magnetic percolation transition) requires lower level of physical NP percolation compared to that governing the IMT.

The last interesting phenomenon found for the cobalt-implanted PI is that the coercive field decreases from 100 to 85 Oe with increase of ion current density from 4 μA×cm^{-2} to 8 or 12 μA×cm^{-2} for the same $F = 1.25 \times 10^{17}$ cm^{-2}. Since, the filling factor of cobalt is the same for these samples, the decrease of H_c must be related to the polymer restructuring and rearrangement of the magnetic phase. As mentioned in the part about FMR studies, the PI samples implanted by high fluences of cobalt showed decrease in effective magnetization. One can suggest that the reason for both decreases should be of the same nature, i.e. the evolution of the polymer structure, in particular, strong carbonization which can facilitate cobalt carbides formation. Additional mechanism can be related to cobalt diffusion and NPs ripening both leading to the dumping of magnetic ordering and weakening of magnetic coupling.

4. CONCLUSIONS

Low-energy implantation of metal ions with high fluences ($\geq 2.5 \times 10^{16}$ cm^{-2}) causes formation of NPs in the shallow polymer layer. The statistically non-uniform distribution of the metal atoms over the depth leads to a size dispersion of NPs. High-fluence implantation also originates the evolution of virgin polymer structure and composition due to the radiation damage. Thus, metals NPs are formed in a strongly carbonized material. Carbonization converts the insulating polymers into conductors.

For cobalt and iron fluence interval between 2.5×10^{16} and ca. 1.0×10^{17} cm^{-2} the dominating mechanism of conductance is found to be VRH similar to the cases of non-metal implantation. Further increase of the fluence leads to the situation where the implanted metal atoms and nucleated particles start contributing to the conductance due to the percolation. IMT is observed for fluence of 1.25×10^{17} cm^{-2} for which the metal filling factor reaches about 0.25 in ca. 100 nm thick surface layer. In these samples the phenomena of weak electron localisation and electron-electron interaction significantly contribute to the charge carrier transport, thus, changing the equations describing the conductivity.

Since cobalt and iron are ferromagnetic materials in bulk, magnetic properties of the nucleated NPs affect the conductance in an external magnetic field leading to appearance of magnetoresistance. This effect is found to be stronger in Fe-implanted polymers compared to those with Co NPs. However, there is good qualitative agreement in the fluence dependence of magnetotransport for both types of metal inclusions. There is also very good correlation with the conventional conductance, i.e. with the IMT transition.

The ensembles of cobalt and iron NPs formed in PI and PET by high-fluence implantation are found to resemble to certain extent properties of thin ferromagnetic granular films. Magnetization of the metal/polymer nanocomposites rises significantly for fluences above 7.5×10^{17} cm^{-2} indicating the magnetic percolation transition. This fluence is lower compared to that which is required for the percolation transition in conductance, thus, indicating magnetic coupling of NPs. SQUID measurements shows that the magnetic coupling in the case of highest implantation fluence of iron (1.25×10^{17} cm^{-2}) leads to ferromagnetic ordering which can withstand room temperature. While for the same fluence of cobalt the samples are found in ferromagnetic state up to blocking temperature of ca. 130K; at higher temperature the composites experience transition to superparamagnetic state.

REFERENCES

[1] A. Meldrum, R.F. Haglund Jr., L.A. Boatner and C.W. White // *Adv. Mater.* **13** (2001) 1431.

[2] A.L. Stepanov, In: *Metal-Polymer Nanocomposites*, ed. by L. Nicolais and G. Carotenuto (J. Wiley & Sons: New York, 2005), p. 241.

[3] A.L. Stepanov and V.N. Popok // *Surf. Coat. Technol.* **185** (2004) 30.

[4] P. Gambardella, S. Rusponi, M. Verones, S. Dhesi, C. Grazioli, A. Dallmeyer, I. Cabria, R. Zeller, P.H. Dederichs, K. Kern, C. Carbone and H. Brune // *Science* **300** (2003) 1130.

[5] J. Nogues, J. Sort, V. Langlais, V. Skumryev, S. Surinach, J.S. Munoz and M.D. Baro // *Phys. Rep.* **422** (2005) 65.

[6] W.J.M. Naber, S. Faez and W.G. van der Wiel // *J. Phys. D: Appl. Phys.* **40** (2007) R205.

[7] R.I. Khaibullin, B.Z. Rameev, C.Okay, A.L. Stepanov, V.A. Zhikharev, I.B. Khaibullin, L.R. Tagirov and B. Aktas, In: *Nanostructured Magnetic Materials and Their Applications, NATO Science Series: II Mathematics, Physics and Chemistry*, V. 143, ed. by B. Aktas, L. Tagirov and F. Mikailov (Kluwer: Dordrecht, 2004), p.33.

[8] A. Meldrum, R. Lopez, R.H. Magruder, L.A. Boatner and C.W. White, In: *Materials Science with Ion Beams*, ed. by H. Bernas (Springer-Verlag: Berlin, 2010), p. 255; G. Mattei, P. Mazzoldi and H. Bernas, *ibidem,* p. 287.

[9] T. Venkatesan, L. Calcagno, B.S. Elman and G. Foti, In: *Ion Beam Modification of Insulators*, ed. by P. Mazzoldi and G.W. Arnold (Elsevier: Amsterdam, 1987), p. 301.

[10] V.N. Popok // *Surf. Investigations* **14** (1999) 843.

[11] M. Behar and D. Fink, In: *Fundamentals of Ion-Irradiated Polymers,* ed. by D. Fink (Springer: Berlin, 2004), p. 119.

[12] D.V. Sviridov // *Rus. Chem. Rev.* **71** (2002) 315.

[13] A. Kondyurin and M. Bilek, *Ion Beam Treatment of Polymers* (Elsevier, Amsterdam, 2008).

[14] P.A. Lee and T.V. Ramakrishan, *Rev. Mod. Phys.* **57** (1985) 287.

[15] G. Du, A. Burns, V.N. Prigodin, C.S. Wang, J. Joo and A.J. Epstein // *Phys. Rev. B* **61** (2000) 10142.

[16] V.N. Popok, M.G. Lukashevich, N.I. Gorbachuk, V.B. Odzhaev, R.I. Khaibullin and I.B. Khaibullin // *Phys. Stat. Sol. (a)* **203** (2006) 1545.

[17] C. Okay, B.Z. Rameev, R.I. Khaibullin, M. Okutan, F. Yildiz, V.N. Popok and B. Aktas // *Phys. Stat. Sol. (a)* **203** (2006) 1525.

[18] V.N. Popok, R.I. Khaibullin, V.V. Bazarov, V.F. Valeev, V. Hnatowicz, A. Mackova and V.B. Odzhaev // *Nucl. Instrum. Meth. Phys. Res. B* **191** (2002) 695.

[19] R.I. Khaibullin, V.N. Popok, V.V. Bazarov, E.P. Zheglov, B.Z. Rameev, C. Okay, L.R. Tagirov and B. Aktas // *Nucl. Instrum. Meth. Phys. Res. B* **191** (2002) 810.

[20] A. Mackova, V. Hnatowicz, V. Peřina, V.N. Popok, R.I. Khaibullin, V.V. Bazarov and V.B. Odzhaev // *Surf. Coat. Technol.* **158-159** (2002) 395.

[21] V.N. Popok, R.I. Khaibullin, A. Toth, V. Beshliu, V. Hnatowicz and A. Mackova // *Surf. Sci.* **532-535** (2003) 1034.

[22] B. Rameev, C. Okay, F. Yildizm R.I. Khaibullin, V.N. Popok and B. Aktas // *J. Magnet. Magn. Mater.* **278** (2004) 164.

[23] V.N. Popok, M.G. Lukashevich, S.M. Lukashevich, R.I. Khaibullin and V.V. Bazarov // *Surf. Sci.* **566-568** (2004) 327.

[24] M.G. Lukashevich, X. Batlle, A. Labarta, V.N. Popok, V.A. Zhikharev, R.I. Khaibullin and V.B. Odzhaev // *Nucl. Instrum. Meth. Phys. Res. B* **257** (2007) 589.

[25] M.G. Lukashevich, V.N. Popok, V.S. Volobuev, A.A. Melnikov, R.I. Khaibullin, V.V. Bazarov, A. Wieck and V.B. Odzhaev // *Open Appl. Phys. J.* **3** (2010) 1.

[26] A. Kharchenko, M. Lukashevich, V. Popok, R. Khaibullin, V. Valeev, V. Bazarov, O. Petracic, A. Wieck and V. Odzhaev // *Part. Part. Syst. Char.* **30** (2013) 180.

[27] V.N. Popok, In: *Surface Science Research*, ed. by C.P. Norris (Nova Science Publ.: New York, 2005), p. 147.

[28] G. Marletta, In: *Materials Science with Ion Beams,* ed. by H. Bernas (Springer-Verlag: Berlin, 2010), p. 345.

[29] E.H. Lee // *Nucl. Instrum. Meth. Phys. Res. B* **151** (1999) 29.

[30] G. Marletta and F. Iacona, In: *Materials and Processes for Surface and Interface Engineering*, ed. by Y. Pauleau (Kluwer, Dordrecht, 1995), p. 597.

[31] G. Marletta and F. Iacona // *Nucl. Instrum. Meth. Phys. Res. B* **80/81** (1993) 1405.

[32] V.N. Popok, I.I. Azarko, R.I. Khaibullin, A.L. Stepanov, V. Hnatowicz, A. Mackova and S.V. Prasalovich // *Appl. Phys. A* **78** (2004) 1067.

[33] V. Švorčik, R. Endršt, V. Rybka, V. Hnatowicz and F. Černy // *J. Electrochem. Soc.* **141** (1994) 582.

[34] V.B. Odzhaev, I.P. Kozlov, V.N. Popok and D.V. Sviridov, *Ion Implantation of Polymers* (Belorussian State University: Minsk, 1998).

[35] P. Apel, A. Schulz, R. Spohr, C. Trautmann and V. Vutsadakis // *Nucl. Instrum. Meth. Phys. Res. B* **131** (1997) 55.

[36] A. Mackova, J. Bocan, R.I. Khaibullin, V.F. Valeev, P. Slepicka, P. Sajdl and V. Svorcik // *Nucl. Instrum. Meth. Phys. Res. B* **267** (2009) 1549.

[37] A. Mackova, P. Malinsky, R. Miksova, H. Pupikova, R.I. Khaibullin, V.F. Valeev,

V. Svorcik and P. Slepicka // *Nucl. Instrum. Meth. Phys. Res. B* **307** (2013) 598.

[38] V.B. Odzhaev, I.I. Azarko, I.A. Karpovich, I.P. Kozlov, V.N. Popok, D.V. Sviridov, V. Hnatowicz, O.N. Jankovskij, V. Rybka and V. Švorčik // *Mater. Lett.* **23** (1995) 163.

[39] A. Kondyurin, B.K. Gan, M.M.M. Bilek, D.R. McKenzie, K. Mizuno and R. Wuhrer // *Nucl. Instrum. Meth. Phys. Res. B* **266** (2008) 1074.

[40] V.N. Popok, I.I. Azarko, V.B. Odzhaev, A. Toth and R.I. Khaibullin // *Nucl. Instrum. Meth. Phys. Res. B* **178** (2001) 305.

[41] V.N. Popok, I.A. Karpovich, V.B. Odzhaev and D.V. Sviridov // *Nucl. Instrum. Meth. Phys. Res. B* **148** (1999) 1106.

[42] R. Nathawat, Y.K. Vijay, P. Kumar, P. Kulriya, V. Ganesan and V. Sathe // *Adv. Polymer Technol.* **27** (2008) 143.

[43] N.C. Koon, D. Weber, P. Pehrsson and A.I. Schindler // *Mater. Res. Soc. Symp. Proc.* **27** (1984) 445.

[44] P.E. Pehrsson, D.C. Weber, N.C. Koon, J.E. Campana and S.L. Rose // *Mater. Res. Soc. Symp. Proc.* **27** (1984) 429.

[45] A. Moliton, B. Lucas, C. Moreau, R.H. Friend and B. Francois // *Philos. Mag. B* **69** (1994) 1155.

[46] Y. Wang, S.S. Mohite, L.B. Bridwell, R.E. Giedd and C.J. Sofield // J. Mater. Res. **8** (1993) 388.

[47] B. Wasserman // *Phys. Rev. B* **34** (1986) 1926.

[48] J. Davenas and P. Thevenard // *Nucl. Instrum. Meth. Phys. Res. B* **80/81** (1993) 1021.

[49] T. Chen S. Yao, K. Wang, H. Wang, S. Zhou // *Surf. Coat. Technol.* **203** (2009) 3718.

[50] N.F. Mott and E.A. Devis, *Electronic Processes in Non-Crystalline Materials* (Clarendon: Oxford, 1979).

[51] Y. Wang, L.B. Bridwell and R.E. Giedd // *J. Appl. Phys.* **73** (1993) 474.

[52] S. Vionnet-Menot, C. Grimaldi, T. Maeder, S. Strässler and P. Ryser // *Phys. Rev. B* **71** (2005) 064201.

[53] W. Schirmacher // *Phys. Rev. B* **41** (1990) 2461.

[54] B.L. Altshuler, A.G. Aronov and P.A. Lee // *Phys. Rev. Lett.* **44** (1980) 1288.

[55] G. Du, N.N. Prigodin, A. Burns, J. Joo, C.S. Wang and A.J. Epstein // *Phys. Rev. B* **58** (1998) 4485.

[56] K.Z. Suzuki, H. Yanagihara, T. Niizeki, K. Kojio and E. Kita // *Appl. Phys. Lett.* **101** (2012) 222401.

[57] T.-X. Chen, S. Yao, W. Hua, T. Fa, L. Li and S.-Q. Zhou // *Chin. Phys. Lett.* **26** (2009) 087201.

[58] G.V. Skrotskii and L.V. Kurbatov, In: *Ferromagnetic Resonance*, edited by S.V. Vonsovskii (Pergamon: Oxford, 1966), p. 345.

[59] B.X. Liu, J. Wang and Z.Z. Fang // *J. Appl. Phys.* **69** (1991) 7342.

[60] J.-J. Delaunay, T. Hayashi, M. Tomita and S. Hirono // *J. Appl. Phys.* **82** (1997) 2200.

[61] K.H. Heining, T. Muller, B. Schmidt, M. Strobel and W. Moller // *Appl. Phys. A* **77** (2003) 17.

[62] J.L. Dormann, D. Fiorani and E. Tronc // *Adv. Chem. Phys.* **98** (1997) 283.